Spin-dependent tunneling in 2D MnBi$_2$Te$_4$-based magnetic tunnel junctions

Guohui Zhan, Zhilong Yang, Kun Luo, Dong Zhang, Wenkai Lou, Jiangtao Liu,* Zhenhua Wu,*[ID] and Kai Chang*

Magnetic tunnel junctions (MTJs) with ferromagnetic (FM) and/or antiferromagnetic (AFM) materials have attracted wide interest for their promising application in spintronic devices. Recently, many discovered two-dimensional (2D) magnetic materials offer a flexible platform to design switchable layered FM/AFM MTJs. By using the first-principles quantum transport simulations, we designed the MTJs based on 2D van der Waals layered MnBi$_2$Te$_4$ and studied the spin-dependent electronic and transport properties of the MTJs with the different thickness MnBi$_2$Te$_4$ as well as their FM and AFM configurations. As the increment of MnBi$_2$Te$_4$ layers, our results show that there is a higher spin polarization and the tunnel magnetoresistance (TMR) ratio at the Fermi level correspondingly increases: 100% and 500%. In particular, when the spin–orbit coupling (SOC) is accounted, the TMR ratio can be enhanced to 500% and 4000%, indicating the SOC effect can lead to the performance improvement of MnBi$_2$Te$_4$-based MTJs.

Impact statement

For Moore's Law to continue to work, there is an urgent demand to find new principles, new materials, and more concepts for future devices. Among them, spintronics has exhibited great potential due to its excellent performance. A typical widely used device is the magnetic tunnel junction (MTJ) in spintronics. Recently, more and more MTJs based on discovered two-dimensional magnetic materials have been predicted with higher tunnel magnetoresistance (TMR). As the first magnetic topological materials, MnBi$_2$Te$_4$ hold various magnetic states and thickness-dependent properties rather than single ferromagnetic states, and there are more possibilities to design versatile MTJ devices. Here, we construct the magnetic tunnel junctions based on MnBi$_2$Te$_4$ with Cu as the electrode: Cu/n-Layer-MnBi$_2$Te$_4$/Cu (n = 1, 2, 3, 4) device. Based on density functional theory and nonequilibrium Green's function, we found that with the thickening of the MnBi$_2$Te$_4$ layers, the spin filtering of MnBi$_2$Te$_4$ is more apparent, where the TMR value at the Fermi level is 100%, 200%, and 500% for n = 2, 3, 4 in Cu/n-Layer-MnBi$_2$Te$_4$/Cu devices, respectively. In particular, when the spin–orbit coupling (SOC) is accounted, the TMR ratio can be enhanced to 500%, 4000% for n = 2, 4, indicating the SOC effect can lead to the performance improvement of MnBi$_2$Te$_4$-based MTJs. We believe that our results can motivate further studies on MnBi$_2$Te$_4$-based MTJs for future spintronics devices.

Introduction

Spintronics has exhibited great potential and played an important role due to unique properties, rather than conventional electronic devices, such as nonvolatility and lower consumption. A typical widely used device is the magnetic tunnel junction in spintronics. How to improve performance, such as tunnel magnetoresistance (TMR), has always been an important and hot topic in MTJs. The TMR ratio is one of the important properties of MTJs and a higher ratio indicates a better performance. Since the 1970s, a lot of efforts have been devoted to achieving a high TMR ratio.[1–13] Miyazaki et al. and Moodera et al. independently found a giant magnetic tunneling effect in (Co)Fe/Al$_2$O$_3$/(Co)Fe junctions at room temperature.[2,3] Subsequently, large values of TMR were also observed in crystalline MTJs with MgO barriers.[5,7,10,11,13] Nowadays, MTJ becomes one of the most important spintronics applications, which can be used as a fundamental component in many spintronic devices, such as magnetic sensor[14] and magnetoresistive random-access memory (MRAM) devices.[15,16]

To further improve the performance and reduce the size, van der Waals (vdW) two-dimensional (2D) materials have attracted extensive attention in recent years, due to new physics arising from the atomic structure and flexible layered configurations. Compared with the usual

Guohui Zhan, Institute of Microelectronics, Chinese Academy of Sciences, Beijing, China; University of Chinese Academy of Sciences, Beijing, China
Zhilong Yang, National Laboratory of Solid State Microstructures, School of Physics, Nanjing University, Nanjing, China
Kun Luo, Institute of Microelectronics, Chinese Academy of Sciences, Beijing, China; University of Chinese Academy of Sciences, Beijing, China
Dong Zhang, SKLSM, Institute of Semiconductors, Chinese Academy of Sciences, Beijing, China
Wenkai Lou, SKLSM, Institute of Semiconductors, Chinese Academy of Sciences, Beijing, China
Jiangtao Liu, School of Mechatronics Engineering, Guizhou Minzu University, Guiyang, China; jtliu@semi.ac.cn
Zhenhua Wu, Institute of Microelectronics, Chinese Academy of Sciences, Beijing, China; University of Chinese Academy of Sciences, Beijing, China; wuzhenhua@ime.ac.cn
Kai Chang, SKLSM, Institute of Semiconductors, Chinese Academy of Sciences, Beijing, China; kchang@semi.ac.cn
*Corresponding author

three-dimensional (3D) materials, 2D materials have a natural advantage of ultrathin to the atomic scale and are connected by vdW interaction without chemical bonding. In recent years, more and more 2D vdW crystals have been experimentally found to be ferromagnetic, such as $Cr_2Ge_2Te_6$,[17] CrX_3 (X = Cl, Br, I),[18–20] Fe_3GeTe_2,[21] VSe_2,[22] $MnBi_2Te_4$[23] , etc. Some of them have been theoretically predicted and experimentally verified to be good candidates for magnetic tunnel junctions.[24–37] For example, Song et al. found that few-layer antiferromagnetic (AFM) CrI_3 can transfer to a FM state by an external magnetic field, resulting in large spin polarization and giant tunneling magnetoresistance in spin-filter vdW heterostructures.[25] More than 1000% TMR ratio in MTJ-based Fe_3GeTe_2 electrode is predicted by Li et al.[27] In addition, most 2D materials have stronger magnetism oriented out-of-plane, indicating that it has perpendicular magnetic anisotropy (PMA) and can be made for perpendicular MTJs (pMTJs).[38]

In 2019, $MnBi_2Te_4$ was first confirmed to be intrinsic magnetic topological insulators.[23,39–41] As a versatile magnetic material, it holds various properties that can be realized to quantum anomalous Hall (QAH) effect, antiferromagnetic topological insulator, magnetic axion insulator, and tunable dynamical axion field.[42–46] Yan et al. found a high 4000% TMR ratio and almost 100% spin filtering ratio in $MnBi_2Te_4|h$-BN$|MnBi_2Te_4$ MTJ.[35] However, $MnBi_2Te_4$-based MTJs with different magnetic states and spin–orbit coupling effect have not been studied. Here, we construct the magnetic tunnel junctions based on $MnBi_2Te_4$ (MBT) with Cu as the electrode: Cu/n-Layer-MBT/Cu (n = 1, 2, 3, 4) device. Based on density functional theory (DFT) and nonequilibrium Green's function (NEGF), we have studied the spin-dependent tunneling of MTJs based on different thickness MBT films. Our transport calculations show that there is about 80% spin polarization in a Cu/single-layer-MBT/Cu device. With the thickening of the MBT layers, the spin filtering of MBT is more apparent, where the maximum TMR ratio is 800%, 2500%, and 4000% and the TMR value at the Fermi level is 100%, 200%, and 500% for n = 2, 3, 4 in Cu/n-Layer-MBT/Cu devices, respectively. In addition, we found a larger TMR ratio with the SOC effect. The SOC can lead to the enhancement of spin polarization and TMR ratio in MBT-based MTJs.

The rest of the article is organized as follows. The calculation method and computational details are included in the section "Computational details." In the section "Electronic properties," we investigated the electronic states of MBT and briefly describe the MTJs model-based MBT films. In the section "Results and discussions," we discussed the spin-dependent transport properties of MBT-based devices in detail without and with SOC effect, including the transmission coefficient, conductance, and projected local density of states.

Computational details

The electronic properties of $MnBi_2Te_4$ are obtained by using DFT calculations as implemented in the Vienna Ab Initio Simulation Package (VASP).[47] The exchange–correlation interaction is described by gradient approximation with a Hubbard U parameter (GGA + U,U = 3 eV) approach in the form of the Perdew–Burke–Ernzerhof (PBE) potential.[48] A plane-wave energy cutoff is 450 eV and 8×8×8 Monkhorst grid k points are used for self-consistent calculations.

The spin-dependent transport properties of the MBT-based magnetic tunnel junctions are calculated by using DFT combined with the NEGF formalism,[49,50] as implemented in the Atomistix ToolKit (QuantumATK 2021) software package.[51] A linear combination of atomic orbitals (LCAO) basis with the *PseudoDojo* pseudopotentials was adapted.[52] The optimum geometric structure is also relaxed in QuantumATK, and the vacuum space is more than 15 Å avoiding the image–image interaction. The exchange correlation potential is described by spin-polarized generalized approximation with the Hubbard U (SGGA + U), and the effective Hubbard U parameter (U = 1.8 eV) is applied for Mn 3d orbitals in our quantum transport calculation. The band structure can fit well compared with previous studies and VASP results (see Supplementary Figure S1). A DFT-1/2 method with noncollinear spin–orbit (SOGGA) is used for SOC calculations. The real-space mesh cutoff is taken as 155 Hartree, and 11 × 11 × 151 k-point meshes are used for self-consistent calculations of the electrode region and the central region.

Under the framework of quantum transport, the spin-resolved transmission coefficients are calculated as,

$$T_\sigma(E) = \text{Tr}[\Gamma_{L,\sigma}(E)G_\sigma^r(E)\Gamma_{R,\sigma}(E)G_\sigma^{r\dagger}(E)], \qquad 1$$

where $\Gamma_{L/R,\sigma}$ denotes the coupling between with the left (right) electrode and the central region. $G_\sigma^r(E) = (ES - H - \Sigma_L - \Sigma_R)^{-1}$ is retarded Green's function, where H and S represent the Hamiltonian and the overlap matrices, respectively. $\Sigma_{L/R}$ is the self-energy and σ is the spin label.

Electronic properties

The structure of $MnBi_2Te_4$ is illustrated in **Figure** 1a–b. $MnBi_2Te_4$ has a layered crystal structure with a triangle lattice from the top view, the materials consist of septuple layers (SL) arranged along the z direction, and every SL is connected by the vdW interaction. The magnetic Mn atom whose magnetic moment is roughly 5 μ_B locates at the center of the SL (the red arrow denotes the spin moment of Mn in Figure 1b). The optimized lattice parameter is $a = b = 4.371$ Å, which is almost consistent with the experimental data.[23] The structure of nonmagnetic $MnBi_2Te_4$ is described by the space group D_{3d}^5 (No. 166), which contains inversion symmetry P, threefold rotation symmetry C_{3z} , and twofold rotation symmetry C_{2x} . It's
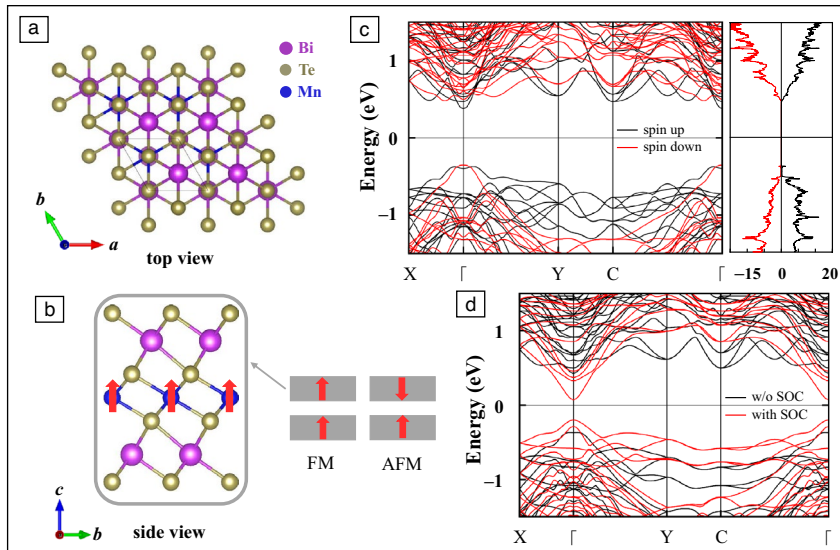
Figure 1. Crystal and electronic structure of magnetic $MnBi_2Te_4$. (a) Top and (b) side views of the atomic lattice of bulk $MnBi_2Te_4$; the structure consists of septuple layers. The red arrow denotes the direction of the magnetic moment of the Mn atom. The parallel and antiparallel magnetism stand for ferromagnetic (FM) and antiferromagneic (AFM) states, respectively. (c) Band structures and spin-resolved density of states of FM state in MBT films, where black and red lines denote spin-up and spin-down, respectively. (d) Band structures of AFM state in MBT films without and with spin–orbit coupling. The black and red lines represent the band feature without and with the SOC effect, respectively.

is 5.1 percent. The geometry relaxation of the Cu/single-layer-MBT/Cu device gives that the distance from $MnBi_2Te_4$ surface Te atoms to the Cu surface layer along the z direction is about 2.6217 Å and 2.6226 Å, respectively. To check the stability of the vdW interfaces, we also calculated the binding energy of the Cu/MBT heterojunction, which is defined as:

$$E_B = E(Cu/MBT) - E(Cu) - E(MBT),$$
$$2$$

where E is the total energy. Our calculations show that the E_B is negative for all MBT-based MTJs in this work (see Supplementary Tables S2, S3), indicating the interfaces of the MTJ model are stable.

We first investigated the spin-dependent carrier transmission through a single-layer MBT film sandwiched between two Cu electrodes, where MBT serves as an ultrathin spin filter. The spin-resolved transmission spectrum of the Cu/single-layer-MBT/Cu system is depicted in Figure 2c. The transport calculations show an obvious spin polarization that the spin-up channel is greater than the spin-down channel, especially if the energy is less than -0.5 eV (the Fermi energy is set to zero). The majority spin is the spin-up channel, and we can define the spin polarization value: $\eta = (T_\uparrow(E) - T_\downarrow(E))/(T_\uparrow(E) + T_\downarrow(E))$. When the energy $E < -0.5$ eV, spin polarization η is over 60%; these results mean that MBT is a suitable material for scattering spin filtering. To understand the mechanism of spin filtering, we further calculated the projected local density of states (PLDOS) along the transport direction. There are two sharp peaks ("V"-shape) around the Fermi level, the spin-up and spin-down channels. It reveals that MBT becomes metallic in the presence of Cu, and it comes from the tunneling effect of thin MBT films. When the energy is close to -1 eV, the density of the spin-up channel is obviously larger than the spin-down channel (Figure 2d–e), showing a spin polarization transport along the z direction. The confirmed spin-filter capability of single-layer MBT leads to potential applications in agile MTJ designs by using vdW multilayer MBT.

confirmed as an A-type antiferromagnet with the intralayer ferromagnetic interaction and interlayer antiferromagnetic coupling along the z direction.[23,40,41] We plotted the band structures of the ferromagnetic and the antiferromagnetic $MnBi_2Te_4$ films. Figure 1c shows that the FM state of $MnBi_2Te_4$ film is gapped. From the spin-resolved density of states (DOS), we can find that there exists a large spin polarization below the Fermi level, indicating that it may be used as a good spin filter. The band structures of the AFM state with and without the SOC effect are shown in Figure 1d. The first-principle calculations show that the AFM state of $MnBi_2Te_4$ film is a topologically trivial antiferromagnet without SOC effect. When the SOC is considered, the bandgap is reduced to 0.3 eV. In addition, the magnetic anisotropy energy (MAE) of FM and AFM states was calculated as 1.18 meV and 1.56 meV, indicating that the MBT-based 2D MTJs may hold strong thermal stability.

Results and discussions

Spin-filtering transmission through single-layer-MBT

A simple MBT-based spin-filtering device is shown in **Figure 2**a, the red rectangular frame stands for the central region, metal Cu ($a = b = c = 2.561$ Å, $\alpha = \beta = \gamma = 60°$) is used for the left/right electrode, and Cu (001) surface is matched with single-layer $MnBi_2Te_4$ (0001) surface (Figure 2b). To keep the intrinsic electronic properties of $MnBi_2Te_4$, it's reasonable to strain the Cu surface, and the lattice mismatch of Cu

Cu/n-Layer-MBT/Cu MTJ device

Different thicknesses of MBT films hold different physical properties. For example, 1-SL MBT has FM order, whereas 2-SL MBT is compensated by the AFM state.[53] To explore the different thicknesses effects of MBT-based MTJ, we mainly construct
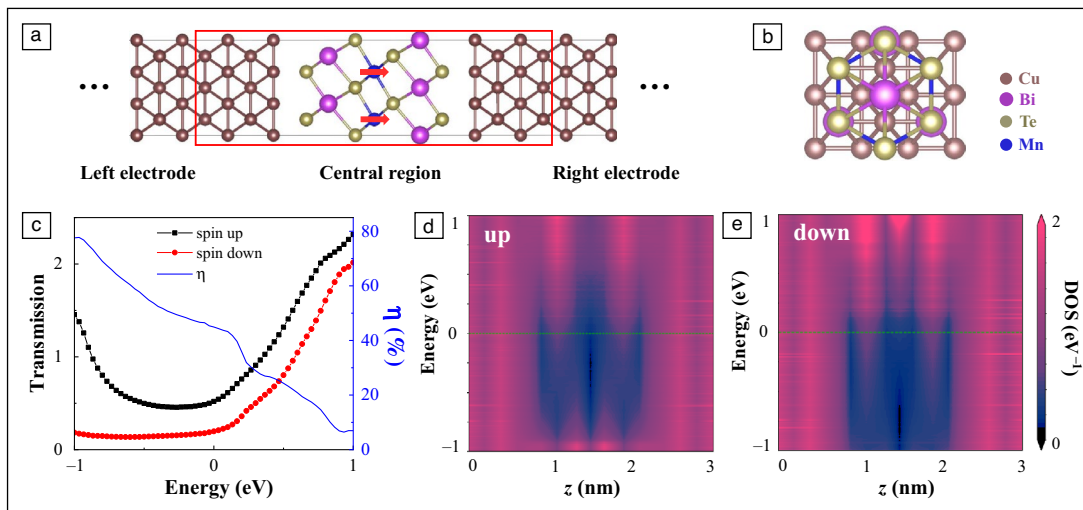
Figure 2. Schematic view of MBT-based device and its transport properties. (a) Cu/single-layer-MBT/Cu device; the red rectangular region represents the central scattering region and Cu is used for the electrode. (b) The interface of Cu (001) surface and MnBi$_2$Te$_4$ (0001) surface from the top view. (c) The spin-resolved transmission spectrum at the equilibrium states. The black and red line points stand for the spin-up and spin-down channel, respectively; the right y-axis shows the spin polarization η. Project local density of states (DOS) along the transport direction of spin-up channel (d) and spin-down channel (e).
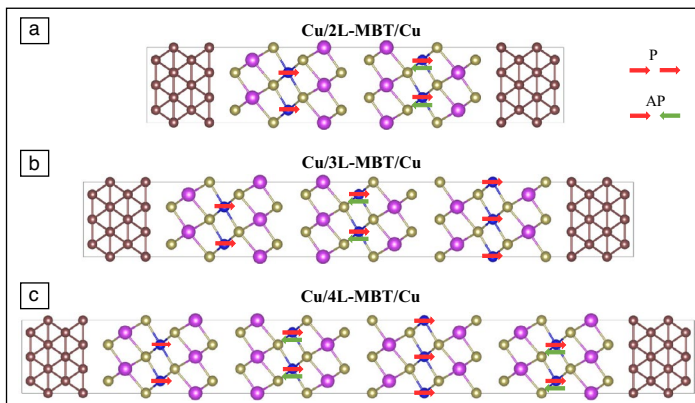

Figure 3. Magnetic tunnel junction devices of Cu/n-Layer-MBT/Cu (n = 2, 3, 4). The red and green arrows represent the magnetic direction of the Mn atom in the parallel (P) and antiparallel (AP) magnetization configurations. These devices are periodic in the x and y direction, and transport is along the z direction.

three types of layered MBT-based MTJs: Cu/n-Layer-MBT/Cu (n = 2, 3, 4) device. The schematic diagram of three MTJ devices is shown in **Figure 3**. The relaxed distance parameters of the Cu/MBT surface of three MTJs are given in Supplementary Table S2. For the Cu/2L-MBT/Cu device, the FM state of MBT films has been defined as the parallel (P) magnetization, and the AFM state denotes the antiparallel (AP) magnetization. The configurations are shown Figure 3; the parallel red arrow represents the P configuration, the antiparallel green arrow stands for AP configuration. The AFM state is the ground state of bulk

MBT. By an external magnetic field or other induced methods, the AFM state (AP configuration) can transfer to the FM state (P configuration), bringing the switching of low resistance and high resistance. Our quantum transport calculations show that three MTJs devices hold similar spin-dependent transport properties. Here, we discussed and compared the spin-dependent transport mechanism of Cu/2L-MBT/Cu and Cu/4L-MBT/Cu devices with the same AFM cell but of different thickness (the similar transport properties of Cu/3L-MBT/Cu can be found in Supplementary Figures S5, S6).

We calculated the spin transmission coefficient within the energy from −0.8 to 0.2 eV for Cu/2L-MBT/Cu and Cu/4L-MBT/Cu devices. At the equilibrium state (or zero voltage bias), the spin-resolved conductance of MTJs as a function of energy is calculated by,

$$G_\sigma(E) = \frac{e^2}{h} \sum_{k_{||}} T_\sigma(k_{||}, E), \qquad 3$$

where $T_\sigma(k_{||}, E)$ is the transmission coefficient with the spin σ. Total conductance of parallel and antiparallel alignment of magnetization of MBT-based MTJs is $G_{P/AP} = G_{P/AP,\uparrow} + G_{P/AP,\downarrow}$, then we can define the TMR ratio: TMR = $(G_P − G_{AP})/G_{AP}$.[27] The conductance and TMR ratio as a function of energy are shown in **Figure 5**. For the Cu/2L-MBT/Cu device, we can obtain that the spin transport transmission of P configuration surpasses the AP configuration, and there is a conductance jump around 0.55 eV due to the large jump spin-resolved density of states in Figure 1c. The maximum TMR ratio is up to 800% at the energy $E_1 = −0.73$ eV, and the TMR value is comparable to the values obtained for the well-known Fe/MgO/Fe MTJ.[5] Furthermore, the TMR gradually decays to 100% with increasing energy. For a better description on the transport
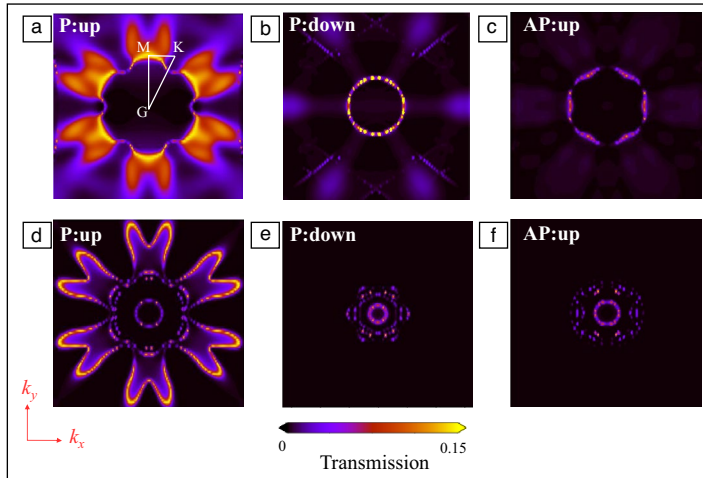
Figure 4. $k_{||}$-resolved electron transmission distribution $T(k_x, k_y, E)$ of two magnetic tunnel junctions (MTJs) for spin-up and spin-down channels in P and AP configuration. (a–c) $E_1 = 0.73$ eV for Cu/2L-MBT/Cu device; (d–f) $E_2 = 0.60$ eV for Cu/4L-MBT/Cu MTJ device.

shows the apparent oscillating behaviors compared to the Cu/2L-MBT/Cu device within the energy range of -0.6 eV and 0.2 eV. Since vacuum layers in between the two anti-magnetization MBT layers serve as the tunneling barriers, there is one tunneling barrier in the Cu/2L-MBT/Cu MTJ and there are three barriers in the Cu/4L-MBT/Cu device, respectively. Thus, the oscillation feature originates from the Fabry–Pérot resonant modes formed between the tunneling barriers due to the multiple reflections between the three barriers in the 4L-MBT region.[54,55] The highest TMR ratio is about 4000% around the energy $E_2 = -0.6$ eV and the TMR is about 500% at the Fermi level. As the MBT films become thicker, the energy points corresponding to the highest TMR value shift to the right. Our results reveal that the thicker thickness of MBT films can effectively enhance the TMR effect.

To obtain better insight into the distinct spin-dependent transport in MBT-based devices, we calculated $k_{||}$-resolved transmission of two MTJ devices at the energies E_1, E_2 in the 2D Brillouin zone (BZ). As shown in **Figure 4**, the left and mid columns show the spin-up and spin-down channels in P configuration, respectively. The right column shows the spin-up channel in AP configuration. Note that the spin-down channel in AP configuration is equivalent to the spin-down channel due to the structural symmetry. We found that the transmission pattern has obvious
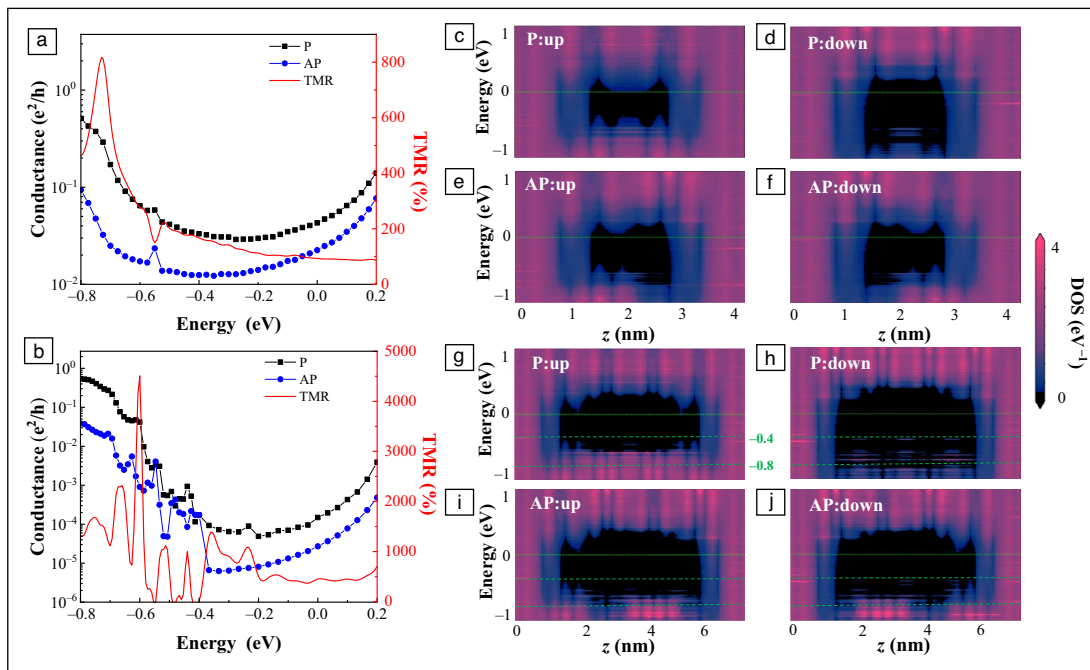
properties around small bias, it's necessary to compare the $TMR(E_F)$ at the Fermi level. By contrast, the transmission spectrum of the Cu/4L-MBT/Cu device holds similar pictures on the whole, where the spin-up channel is almost larger than the spin-down channel. But the conductance of the Cu/4L-MBT/Cu device has a lower spin transport probability and

Figure 5. The spin-resolved conductance, tunnel magnetoresistance (TMR) ratio, and projected local density of states for Cu/2L-MBT/Cu and Cu/4L-MBT/Cu devices. The conductance as a function of energy for Cu/2L-MBT/Cu (a) and Cu/4L-MBT/Cu devices (b) in parallel (P) (black lines) and antiparallel (AP) (blue lines) configurations; (c–f) P and AP configurations of Cu/2L-MBT/Cu device; (g–j) P and AP configurations of Cu/4L-MBT/Cu device. The left and right panels represent the spin-up and spin-down channel, respectively.
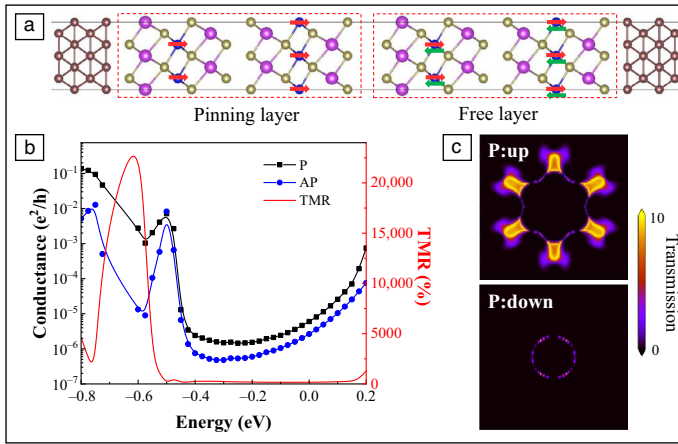
Figure 6. Another Cu/4L-MBT/Cu device and its transport properties. (a) Another Cu/4L-MBT/Cu device model, where red and green arrows represent the magnetic moment of Mn atom. (b) The conductance and tunneling magnetoresistance (TMR) ratio as a function of energy; (c) $k_{||}$-resolved transmission $T(k_x, k_y, E)$ in parallel (P) configuration, where the energy E is –0.6 eV. AP, antiparallel.

hexagonal lattice symmetry: $C_{3z} T(k_{||}) C_{3z}^{\dagger} = T(k_{||})$, the spin-up channel (majority spin) of P configuration (Figure 4a, d) is apparently stronger than the spin-down channel (minority spin) and two spin channels of AP configuration for the two devices. Next, we plotted the PLDOS of P and AP configuration along the transport direction at equilibrium state. As shown in Figure 5c–j, the left and right panels show the spin-up and spin-down channels, respectively. Taking the Cu/2L-MBT/Cu MTJ as an example, in P configuration (Figure 5c–d), there is a majority density of states for the spin-up channel, showing the spin-up channel is of low resistance. In contrast, there are almost no density of states for the spin-down channel, indicating that the spin-down channel is of high resistance. Similar spin-dependent transport properties can also be found in Cu/4L-MBT/Cu MTJ devices.

In addition, the vdW MBT multilayers enable flexible layer-resolved magnetic configurations. For the previously discussed Cu/4L-MBT/Cu device, the AFM and FM states are realized as AP and P configurations, in which the magnetization direction varies by each layer. There also exist other magnetic arrangements for multilayer MBT films due to various magnetism. Here another Cu/4L-MBT/Cu device with different magnetic alignment is investigated as shown in **Figure** 6a (i.e., each 2L-MBT film holds the same magnetism). The left 2L-MBT films can be used as pinning layers, while the right 2L-MBT can be free layers. To reduce the interlayer magnetic exchange interaction between the left and right 2L-MBT, the vacuum space viewed as a barrier is larger than the former 4L-MBT devices. This MTJ can work by flipping the magnetism of free layers. We investigated the spin transport properties of this MTJ device. Figure 6b shows similar properties compared to Figure 5b. The oscillations in the transmission

are suppressed due to the higher vacuum barriers in the middle. As compared to the former 4L-MBT configuration, the maximum TMR ratio around the energy $E = 0.6$ eV is significantly increased to 20,000% (the transmission spectrum of Figure 6c is significantly higher than that of Figure 4), whereas the TMR ratio at the Fermi level is only 200 percent. These results show that this MTJ type may have poor performance than the former.

Cu/n-Layer-MBT/Cu with SOC effect
The spin–orbit coupling is a relativistic effect that occurs in many materials, and it's essential to take the SOC effect of MnBi$_2$Te$_4$ into account. Therefore, we investigated the spin-dependent transport of MTJ devices in the presence of SOC. As the SOC is accounted, the spin is no longer a good quantum number that spin-up and spin-down are mixed, noncollinear spin is represented as a 2×2 matrix with different mixing of up and down components, the transmission has the form,

$$T = \begin{pmatrix} T_{\uparrow\uparrow} & T_{\uparrow\downarrow} \\ T_{\downarrow\uparrow} & T_{\downarrow\downarrow} \end{pmatrix}. \qquad 4$$

Here, $T_{\uparrow\uparrow}(T_{\downarrow\downarrow})$ represents the spin conserved terms, which means that the electron for left to right with the same spin. $T_{\uparrow\downarrow}(T_{\downarrow\uparrow})$ corresponds to the probability that the spin-up channel will be out scattered with the spin-down channel. **Figure** 7a–b shows the transmission spectrum of a Cu/2L-MBT/Cu device without and with SOC interaction. Without SOC, the spin is conserved (i.e., $T_{\downarrow\uparrow} = 0$). In the presence of the SOC effect, the bandgap becomes smaller, but the up-down component is not zero, indicating that incoming electrons with up (down) spin can be scattered by electrons with down (up) spin. Thus, the spin transport probability with the SOC effect is slightly lower than that without the SOC effect. At last, we calculated the conductance of Cu/2L-MBT/Cu and Cu/4L-MBT/Cu MTJ devices with the SOC effect. Comparing Figures 5a–b and 7c–d, they have a similar tendency, but hold higher maximum TMR value below the Fermi level. And the TMR ratio at the Fermi level also increases from 100 to 500% for the Cu/2L-MBT/Cu device, and from 500 to 4000% for the Cu/4L-MBT/Cu device, respectively. Our calculations show that although the conductance channel is slightly suppressed, the SOC effect can enhance the TMR value of MBT-based MTJs.

Conclusion
In summary, we investigated spin-dependent transport properties of MBT-based devices: Cu/n-Layer MBT/Cu ($n = 1$, 2, 3, 4) by using the DFT-NEGF formalism. There is large spin polarization in the Cu/single-layer MBT/Cu device. As the MBT layer count increases, the spin filtering of MBT is greater, where the TMR (E_F) reaches 100%, 200%, and
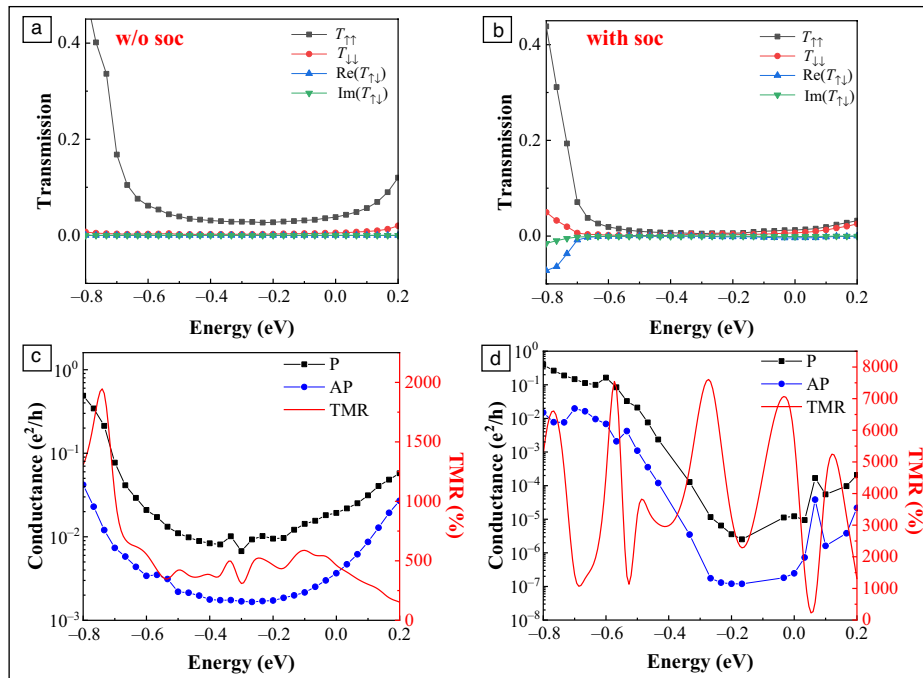
Figure 7. The transmission spectrum, conductance, and tunneling magnetoresistance (TMR) ratio for Cu/2L-MBT/Cu and Cu/4L-MBT/Cu devices. The transmission spectrum $T_{\uparrow\uparrow}, T_{\downarrow\downarrow}, T_{\downarrow\uparrow}$ of Cu/2L-MBT/Cu magnetic tunnel junction devices without (a) and with SOC effect (b). The conductance as a function of energy for Cu/2L-MBT/Cu (c) and Cu/4L-MBT/Cu devices (d) in parallel (P) (black lines) and antiparallel (AP) (blue lines) configuration.

500% for $n = 2, 3, 4$, respectively. In particular, when turning on the SOC effect, the TMR ratio increases from 100% to 500% for Cu/2L-MBT/Cu, and from 500% to 4000% for Cu/4L-MBT/Cu devices, indicating the SOC effect can lead to the enhancement of spin polarization and TMR ratio in MBT-based MTJs. Our results can motivate further studies on MBT-based MTJs for future spintronic devices.

Data availability
Data will be made available on reasonable request.

Conflict of interest
The authors declare no competing financial interest.

Supplementary information
The online version contains supplementary material available at https://doi.org/10.1557/s43577-022-00381-8.

References
1. M. Julliere, *Phys. Lett. A* **54**, 225 (1975). https://doi.org/10.1016/0375-9601(75)90174-7
2. T. Miyazaki, N. Tezuka, *J. Magn. Magn. Mater.* **139**, L231 (1995). https://doi.org/10.1016/0304-8853(95)90001-2
3. J.S. Moodera, L.R. Kinder, T.M. Wong, R. Meservey, *Phys. Rev. Lett.* **74**, 3273 (1995). https://doi.org/10.1103/PhysRevLett.74.3273
4. S.A. Wolf, D.D. Awschalom, R.A. Buhrman, J.M. Daughton, S. von Molnár, M.L. Roukes, A.Y. Chtchelkanova, D.M. Treger, *Science* **294**(5546), 1488 (2001). https://doi.org/10.1126/science.1065389
5. S. Yuasa, T. Nagahama, A. Fukushima, Y. Suzuki, K. Ando, *Nat. Mater.* **3**, 868 (2004). https://doi.org/10.1038/nmat1257
6. T. Marukame, T. Kasahara, K.-I. Matsuda, T. Uemura, M. Yamamoto, *IEEE Trans. Magn.* **41**, 2603 (2005). https://doi.org/10.1109/TMAG.2005.854716
7. D.D. Djayaprawira, K. Tsunekawa, M. Nagai, H. Maehara, S. Yamagata, N. Watanabe, S. Yuasa, Y. Suzuki, K. Ando, *Appl. Phys. Lett.* **86**, 092502 (2005). https://doi.org/10.1063/1.1871344
8. M. Oogane, Y. Sakuraba, J. Nakata, H. Kubota, Y. Ando, A. Sakuma, T. Miyazaki, *J. Phys. D* **39**, 834 (2006). https://doi.org/10.1088/0022-3727/39/5/S09
9. H.X. Wei, Q.H. Qin, M. Ma, R. Sharif, X.F. Han, *J. Appl. Phys.* **101**, 09B501 (2007). https://doi.org/10.1063/1.2696590
10. S. Ikeda, J. Hayakawa, Y. Ashizawa, Y.M. Lee, K. Miura, H. Hasegawa, M. Tsunoda, F. Matsukura, H. Ohno, *Appl. Phys. Lett.* **93**, 082508 (2008). https://doi.org/10.1063/1.2976435
11. S. Tsunegi, Y. Sakuraba, M. Oogane, K. Takanashi, Y. Ando, *Appl. Phys. Lett.* **93**, 112506 (2008). https://doi.org/10.1063/1.2987516
12. L. Jiang, H. Naganuma, M. Oogane, Y. Ando, *Appl. Phys. Express* **2**, 083002 (2009). https://doi.org/10.1143/APEX.2.083002
13. S. Ikeda, K. Miura, H. Yamamoto, K. Mizunuma, H. Gan, M. Endo, S. Kanai, J. Hayakawa, F. Matsukura, H. Ohno, *Nat. Mater.* **9**, 721 (2010). https://doi.org/10.1038/nmat2804
14. Y. Wang, J. Li, D. Viehland, *Mater. Today* **17**, 269 (2014). https://doi.org/10.1016/j.mattod.2014.05.004
15. R.W. Dave, G. Steiner, J.M. Slaughter, J.J. Sun, B. Craigo, S. Pietambaram, K. Smith, G. Grynkewich, M. DeHerrera, J. Akerman, S. Tehrani, *IEEE Trans. Magn.* **42**, 1935 (2006). https://doi.org/10.1109/TMAG.2006.877743
16. G. Grynkewich, J. Åkerman, P. Brown, B. Butcher, R.W. Dave, M. DeHerrera, M. Durlam, B.N. Engel, J. Janesky, S. Pietambaram, N.D. Rizzo, J.M. Slaughter, K. Smith, J.J. Sun, S. Tehrani, *MRS Bull.* **29**(11), 818 (2004). https://doi.org/10.1557/mrs2004.234
17. C. Gong, L. Li, Z. Li, H. Ji, A. Stern, Y. Xia, T. Cao, W. Bao, C. Wang, Y. Wang, Z.Q. Qiu, R.J. Cava, S.G. Louie, J. Xia, X. Zhang, *Nature* **546**, 265 (2017). https://doi.org/10.1038/nature22060
18. B. Huang, G. Clark, E. Navarro-Moratalla, D.R. Klein, R. Cheng, K.L. Seyler, D. Zhong, E. Schmidgall, M.A. McGuire, D.H. Cobden, W. Yao, D. Xiao, P. Jarillo-Herrero, X. Xu, *Nature* **546**, 270 (2017). https://doi.org/10.1038/nature22391
19. D.R. Klein, D. MacNeill, J.L. Lado, D. Soriano, E. Navarro-Moratalla, K. Watanabe, T. Taniguchi, S. Manni, P. Canfield, J. Fernández-Rossier, P. Jarillo-Herrero, *Science* **360**(6394), 1218 (2018). https://doi.org/10.1126/science.aar3617
20. W. Chen, Z. Sun, Z. Wang, L. Gu, X. Xu, S. Wu, C. Gao, *Science* **366**, 983 (2019). https://doi.org/10.1126/science.aav1937
21. Y. Deng, Y. Yu, Y. Song, J. Zhang, N.Z. Wang, Z. Sun, Y. Yi, Y.Z. Wu, S. Wu, J. Zhu, J. Wang, X.H. Chen, Y. Zhang, *Nature* **563**, 94 (2018). https://doi.org/10.1038/s41586-018-0626-9
22. M. Bonilla, S. Kolekar, Y. Ma, H.C. Diaz, V. Kalappattil, R. Das, T. Eggers, H.R. Gutierrez, M.-H. Phan, M. Batzill, *Nat. Nanotechnol.* **13**, 289 (2018). https://doi.org/10.1038/s41565-018-0063-9

23. Y. Gong, J. Guo, J. Li, K. Zhu, M. Liao, X. Liu, Q. Zhang, L. Gu, L. Tang, X. Feng, D. Zhang, W. Li, C. Song, L. Wang, P. Yu, X. Chen, Y. Wang, H. Yao, W. Duan, Y. Xu, S.-C. Zhang, X. Ma, Q.-K. Xue, K. He, *Chin. Phys. Lett.* **36**(7), 076801 (2019). https://doi.org/10.1088/0256-307X/36/7/076801

24. H. Zhang, M. Ye, Y. Wang, R. Quhe, Y. Pan, Y. Guo, Z. Song, J. Yang, W. Guo, J. Lu, *Phys. Chem. Chem. Phys.* **18**, 16367 (2016). https://doi.org/10.1039/C6CP01866A

25. T. Song, X. Cai, M.W.-Y. Tu, X. Zhang, B. Huang, N.P. Wilson, K.L. Seyler, L. Zhu, T. Taniguchi, K. Watanabe, M.A. McGuire, D.H. Cobden, D. Xiao, W. Yao, X. Xu, *Science* **360**(6394), 1214 (2018). https://doi.org/10.1126/science.aar4851

26. Z. Wang, I. Gutiérrez-Lezama, N. Ubrig, M. Kroner, M. Gibertini, T. Taniguchi, K. Watanabe, A. Imamoğlu, E. Giannini, A.F. Morpurgo, *Nat. Commun.* **9**, 2516 (2018). https://doi.org/10.1038/s41467-018-04953-8

27. X. Li, J.-T. Lu, J. Zhang, L. You, Y. Su, E.Y. Tsymbal, *Nano Lett.* **19**, 5133 (2019). https://doi.org/10.1021/acs.nanolett.9b01506

28. Z.-Z. Lin, X. Chen, *Adv. Electron. Mater.* **6**, 1900968 (2020). https://doi.org/10.1002/aelm.201900968

29. Z. Yan, R. Zhang, X. Dong, S. Qi, X. Xu, *Phys. Chem. Chem. Phys.* **22**, 14773 (2020). https://doi.org/10.1039/D0CP02534H

30. L. Zhang, T. Li, J. Li, Y. Jiang, J. Yuan, H. Li, *J. Phys. Chem. C* **124**, 27429 (2020). https://doi.org/10.1021/acs.jpcc.0c09432

31. W. Yang, Y. Cao, J. Han, X. Lin, X. Wang, G. Wei, C. Lv, A. Bournel, W. Zhao, *Nanoscale* **13**, 862 (2021). https://doi.org/10.1039/D0NR07290G

32. N. Devaraj, K. Tarafder, *Phys. Rev. B* **103**, 165407 (2021). https://doi.org/10.1103/PhysRevB.103.165407

33. Y. Zhu, X.Y. Guo, L.N. Jiang, Z.R. Yan, Y. Yan, X.F. Han, *Phys. Rev. B* **103**, 134437 (2021). https://doi.org/10.1103/PhysRevB.103.134437

34. X. Guo, B. Yang, X. Zhang, Y. Zhu, X. Han, Y. Yan, *Phys. Rev. B* **104**, 144423 (2021). https://doi.org/10.1103/PhysRevB.104.144423

35. Z. Yan, X. Jia, X. Shi, X. Dong, X. Xu, *Appl. Phys. Lett.* **118**, 223503 (2021). https://doi.org/10.1063/5.0052720

36. S. Parkin, *MRS Bull.* **31**(5), 389 (2006). https://doi.org/10.1557/mrs2006.99

37. W. Savero Torres, J.F. Sierra, L.A. Benítez, F. Bonell, J.H. García, S. Roche, S.O. Valenzuela, *MRS Bull.* **45**(5), 357 (2020) https://doi.org/10.1557/mrs.2020.121

38. B. Dieny, M. Chshiev, *Rev. Mod. Phys.* **89**, 025008 (2017). https://doi.org/10.1103/RevModPhys.89.025008

39. M.M. Otrokov, I.I. Klimovskikh, H. Bentmann, D. Estyunin, A. Zeugner, Z.S. Aliev, S. Gaß, A.U.B. Wolter, A.V. Koroleva, A.M. Shikin, M. Blanco-Rey, M. Hoffmann, I.P. Rusinov, A.Yu. Vyazovskaya, S.V. Eremeev, Yu.M. Koroteev, V.M. Kuznetsov, F. Freyse, J. Sánchez-Barriga, I.R. Amiraslanov, M.B. Babanly, N.T. Mamedov, N.A. Abdullayev, V.N. Zverev, A. Alfonsov, V. Kataev, B. Büchner, E.F. Schwier, S. Kumar, A. Kimura, L. Petaccia, G. Di Santo, R.C. Vidal, S. Schatz, K. Kißner, M. Ünzelmann, C.H. Min, S. Moser, T.R.F. Peixoto, F. Reinert, A. Ernst, P.M. Echenique, A. Isaeva, E.V. Chulkov, *Nature* **576**, 416 (2019). https://doi.org/10.1038/s41586-019-1840-9

40. D. Zhang, M. Shi, T. Zhu, D. Xing, H. Zhang, J. Wang, *Phys. Rev. Lett.* **122**, 206401 (2019). https://doi.org/10.1103/PhysRevLett.122.206401

41. J. Li, Y. Li, S. Du, Z. Wang, B.-L. Gu, S.-C. Zhang, K. He, W. Duan, Y. Xu, *Sci. Adv.* **5**, eaaw5685 (2019). https://doi.org/10.1126/sciadv.aaw5685

42. Y. Li, J. Xiao, K. Chang, *Nano Lett.* **18**, 3032 (2018). https://doi.org/10.1021/acs.nanolett.8b00492

43. Y. Deng, Y. Yu, M.Z. Shi, Z. Guo, Z. Xu, J. Wang, X.H. Chen, Y. Zhang, *Science* **367**, 895 (2020). https://doi.org/10.1126/science.aax8156

44. C. Liu, Y. Wang, H. Li, Y. Wu, Y. Li, J. Li, K. He, Y. Xu, J. Zhang, Y. Wang, *Nat. Mater.* **19**, 522 (2020). https://doi.org/10.1038/s41563-019-0573-3

45. H. Li, C.-Z. Chen, H. Jiang, X.C. Xie, *Phys. Rev. Lett.* **127**, 236402 (2021). https://doi.org/10.1103/PhysRevLett.127.236402

46. B. Wei, J.-J. Zhu, Y. Song, K. Chang, *Phys. Rev. B* **104**, 174436 (2021). https://doi.org/10.1103/PhysRevB.104.174436

47. G. Kresse, J. Furthmüller, *Phys. Rev. B* **54**, 11169 (1996). https://doi.org/10.1103/PhysRevB.54.11169

48. J.P. Perdew, K. Burke, M. Ernzerhof, *Phys. Rev. Lett.* **77**, 3865 (1996). https://doi.org/10.1103/PhysRevLett.77.3865

49. J. Taylor, H. Guo, J. Wang, *Phys. Rev. B* **63**, 245407 (2001). https://doi.org/10.1103/PhysRevB.63.245407

50. M. Brandbyge, J.-L. Mozos, P. Ordejón, J. Taylor, K. Stokbro, *Phys. Rev. B* **65**, 165401 (2002). https://doi.org/10.1103/PhysRevB.65.165401

51. S. Smidstrup, T. Markussen, P. Vancraeyveld, J. Wellendorff, J. Schneider, T. Gunst, B. Verstichel, D. Stradi, P.A. Khomyakov, U.G. Vej-Hansen, M.-E. Lee, S.T. Chill, F. Rasmussen, G. Penazzi, F. Corsetti, A. Ojanperä, K. Jensen, M.L.N. Palsgaard, U. Martinez, A. Blom, M. Brandbyge, K. Stokbro, *J. Phys. Condens. Matter* **32**(1), 015901 (2020). https://doi.org/10.1088/1361-648X/ab4007

52. M. Van Setten, M. Giantomassi, E. Bousquet, M.J. Verstraete, D.R. Hamann, X. Gonze, G.-M. Rignanese, *Comput. Phys. Commun.* **226**, 39 (2018). https://doi.org/10.1016/j.cpc.2018.01.012

53. M.M. Otrokov, I.P. Rusinov, M. Blanco-Rey, M. Hoffmann, A.Y. Vyazovskaya, S.V. Eremeev, A. Ernst, P.M. Echenique, A. Arnau, E.V. Chulkov, *Phys. Rev. Lett.* **122**, 107202 (2019). https://doi.org/10.1103/PhysRevLett.122.107202

54. Z. Wu, F.M. Peeters, K. Chang, *Phys. Rev. B* **82**, 115211 (2010). https://doi.org/10.1103/PhysRevB.82.115211

55. Z. Wu, L. Lin, W. Yang, D. Zhang, C. Shen, W. Lou, H. Yin, K. Chang, *RSC Adv.* **7**, 30963 (2017). https://doi.org/10.1039/c7ra03482b ☐